

Fluorescence and absorption characteristics of *p*-xylene: applicability for temperature measurements

Qianlong Wang¹ · Yuyin Zhang¹ · Liqiao Jiang² · Daiqing Zhao² · Philippe Guibert³ · Shunhua Yang⁴

Received: 31 March 2017 / Accepted: 21 August 2017 / Published online: 30 August 2017
© Springer-Verlag GmbH Germany 2017

Abstract This paper explores the characteristics of absorption and fluorescence spectra of *p*-xylene within the temperature range that is frequently encountered during the mixture formation in internal combustion engines. At 266 nm wavelength, the *p*-xylene absorption cross section shows a mean value of $(3.4 \pm 0.2) \times 10^{-19}$ cm²/molecule within the temperature range from 423 to 623 K in N₂. As expected, fluorescence peak intensity decreases by a factor of 3 when the temperature increases by 100 K, due to a increasing non-radiative decay rate of excited state at increasing temperatures. In addition, the suitability of *p*-xylene for temperature measurements in the gas phase via the single-wavelength

excitation (at 266 nm) two-color detection laser-induced fluorescence imaging is explored. Combinations of spectral detection bands were compared and the combination of 320/289 nm provides the best temperature performance with a relative error of 2.6% within the investigated temperature range. It is also shown that the temperature field measurement has not been strongly affected by the laser attenuation.

1 Introduction

In the context of exploring high-efficiency and clean engine/turbine combustion, the combustion mode, as the homogeneous direct-injection spark-ignition (DISI) is extensively investigated due to its practical advantages compared to port-fuel-injection (PFI) [1, 2]. Since the precise spatio-temporal thermodynamic parameters (concentrations, temperature, fuel-air ratio, etc.) of the eventual spray mixture are crucial to subsequent ignition, flame propagation and pollutant formation, which is a necessary path for engine improvements. To this end, tracer planar laser-induced fluorescence (PLIF) is frequently used for visualization of scalar fields in pre-combustion environments.

A large number of fluorescent tracers are studied for possible thermodynamic indications in according to range dependence of optical methodology. When the spray lies in the liquid and gaseous coexisting stage, laser induced exciplex fluorescence (LIEF) is an ongoing promising technique for two phases measurements. Melton [3] originally explored the naphthalene/tetramethyl-*p*-phenylene diamine (TMPD) tracer couple to spectrally visualize the droplet and vapor phase simultaneously up to temperature of 523 K. Furthermore, Murray and Melton [4] used the same tracer couple to measure droplet temperature through the fluorescence intensity ratio that centred at 500 nm/400 nm within the

✉ Yuyin Zhang
yuyinzhang@sjtu.edu.cn
Qianlong Wang
wangqianlong@sjtu.edu.cn
Liqiao Jiang
jianglq@ms.giec.ac.cn
Daiqing Zhao
Zhaodq@ms.giec.ac.cn
Philippe Guibert
philippe.guibert@upmc.fr
Shunhua Yang
ysh_cardc@126.com

¹ School of Mechanical Engineering, Shanghai JiaoTong University, Shanghai 200240, China
² Guangzhou Institute of Energy Conversion, Chinese Academy of Sciences, Guangzhou 510640, Guangdong, China
³ UPMC Univ Paris 06, CNRS UMR 7190, Institut Jean le Rond d'Alembert, Paris, France
⁴ Science and Technology on Scramjet Laboratory, Hypervelocity Aerodynamics Institute of CARDC, Mianyang 621000, Sichuan, China

temperature range from 298 to 538 K. Lately, varieties of tracer couples were extensively studied and quantitatively investigated, i.e., FB/DEMA [5, 6] and TEA/benzene [7, 8].

After the spray droplet fully evaporated, only gaseous phase exists in the mixture. The optical diagnostic strategy turns to single fluorescing tracer doped to the non-fluorescing single phase mixture. The acetone [9–11] was firstly seeded to nitrogen as the temperature tracer in a heated jet (up to 1000 K) by fluorescence signal excited by the laser of 248/308 nm. Later on, Koch and Hanson [12] reported the 3-pentanone absorption and fluorescence dependence on temperature within range of 300–875 K and a measurement example of temperature and mole fraction fields through 308 and 266 nm excitation in a heated turbulent jet was shown. Einecke et al. [13] doped 3-pentanone to iso-octane to evaluate the temperature, fuel concentration and fuel-air equivalence ratio in a two-stroke engine by a two-line (248 and 308 nm excitation) PLIF within temperature range 350–600 K and a temperature precision of 4% was reported by a single-shot image. Zigan et al. [14] seeded 20% (vol.) of 3-pentanone to iso-octane/ethanol to simultaneously to provide the mixture temperature and vapor distribution in a gasoline spray at ambient pressure and temperature of 0.8 MPa and 673 K. And a maximum local evaporation cooling of 125 K for iso-octane and 150 K for ethanol were found. In general, the ketones have the main advantages of high vapor pressure, visible fluorescence emission and insensitivity of oxygen quenching. However, because of low fluorescence quantum yield (FQY) of ketone, the higher number density of ketone and high density light excitation are required to generate high SNR (fluorescence signal noise ratio) for a reliable measurement.

Since the added ketones may exhibit different chemical characteristics and behaviors to real fuel, some aromatics naturally existing in commercial fuel were also selected to represent the gasoline, diesel or kerosene. In particular, toluene [15–18], TMB (1,2,4-trimethylbenzene) [19], naphthalene and its derivative [21, 22, 28] are widely studied for promising LIF imaging. These organic species commonly have higher FQY in UV range and strong sensitivities to the oxygen concentrations. In the previous studies, the one-ring aromatic hydrocarbons are normally regarded as the gasoline-like tracer, while the two-ring aromatic hydrocarbon is diesel-like. This mainly relies on the similarity properties to the real fuel, e.g., the evaporation characteristics and transport properties. Owing to the distinguishable chemical properties (e.g., volatility) and fluorescence characteristics of ketones and aromatics, the multi-component evaporation and stratification by use of such two kind tracers representing different fuel volatility classes could be readily experimentally studied. Zhang and Sick [23] doped the acetone and *p*-xylene to iso-octane to examine the low and high volatility content evaporation

and distribution characteristics in late injection mode. The experimental results demonstrated that the spatial stratification due to volatility differences was insignificant for acetone and *p*-xylene with various starting conditions. Lately, Williams et al. [24] employed acetone, toluene and TMB to respectively track evaporation characteristics of the light, medium and heavy components of gasoline and indicated that a single tracer was sufficient to give a measure of fuel/air mixing and also of equivalence ratio at later stages in the compression stroke.

Moreover, some diesel-like tracers have received more attention recently. Tea et al. [25] seeded 10% toluene to *n*-dodecane in a diesel jet that operated in pressure range of 4.6–5.3 MPa and temperature range of 623–728 K, where a measured temperature precision of 20–40 K up to 700 K was indicated by the two-line PLIF. Lind et al. [26] further investigated the simultaneous mixture temperature and fuel partial density distribution in a diesel spray operated at 800 K and 5 MPa through seeding 1-methylnaphthalene (1-MN) to nitrogen by the one-line (266 nm excitation) two-color PLIF technique. In addition, other polycyclic aromatic hydrocarbons (PAHs) such as anisole and fluoranthene were also investigated as temperature tracer in the high temperature and high pressure ranges that encountered in an industrial internal combustion engine (ICE). The anisole normally offers the highest absorption cross section and FQY among the one-ring aromatics at the excitation wavelength of 266 nm, which can be regarded as a promising tracer for gasoline temperature measurements in harsh environments [27, 28, 29]. On the other hand, owing to satisfactory fluorescence signals within the large temperature and pressure range by two excitation wavelengths of 266 and 355 nm, fluoranthene was also studied and its photophysical characteristics were thoroughly documented [30].

In the present article, vapor *p*-xylene absorption characteristics within the range of 240–300 nm and its fluorescence spectrum evolution with temperature that excited by 266 nm are documented. Based on these fluorescence results, the implication for temperature measurements using the single excitation two-color detection PLIF technique is exploited and validated for the first time. Three fluorescence spectral bands that respectively centred at $\Delta\lambda_1 = 289$ nm, $\Delta\lambda_2 = 320$ nm and $\Delta\lambda_3 = 340$ nm are selected to conceive three spectral band combinations (320/289 nm, 340/289 nm and 340/320 nm) for the temperature measurements. These comparisons help to optimize the spectral band combination for rendering the best temperature measurement performance. Additionally, these data could be regarded as complements of toluene and 1,2,4-trimethylbenzene database, which helps us optimize the tracer in gasoline surrogate fuel studies.

2 Experimental implementation

2.1 Selection of the tracer

(Para-) *p*-xylene is one of the three isomeric forms of xylene. Other two isomers are distinguished by the designations *ortho*- (*o*-), *meta*- (*m*-), which specifies by the position of two methyl groups are attached to the benzene ring. In the current paper, the *p*-xylene has been retained to further investigation. One reason is that it naturally exists in the gasoline. In the standard gasoline, there exists 4.73% of the toluene, 3.26% of TMB and 9.65% of xylene (in weight) [31]. Therefore, its distribution is a direct representative of medium-boiling component of gasoline [23]. Secondly, as the *p*-xylene is regarded as a potential tracer for temperature and fuel concentration measurements via PLIF technique, but the photophysical behavior information, such as absorption cross section, and also the evolution of fluorescence spectrum with temperature and FQY, is insufficient. Thus, these photophysical information of *p*-xylene are the complements of that of toluene and TMB, which offers an

alternative tracer option for gasoline and its surrogate studies. Eventually, due to similar thermodynamic properties to primary reference fuel (PRF), it is verified that its evaporation behavior could represent the low volatile component of *n*-octane in two-component (*n*-octane 50% and *n*-tridecane 50%) fuel spray evaporation process via the LAS (laser absorption scattering) technique in the previous studies [32]. The thermodynamic properties of pure *p*-xylene (C_6H_{10}), *n*-octane (C_8H_{18}) and gasoline are summarized in Table 1.

2.2 Experimental setup

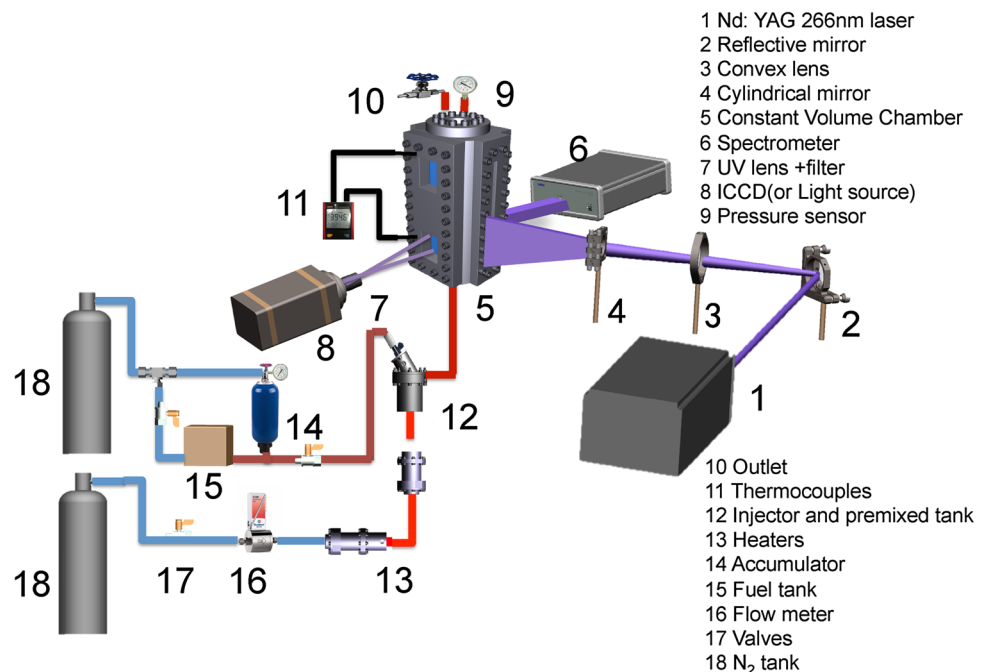
The absorption, fluorescence spectrum and fluorescence signal field (temperature field) measurements of gaseous *p*-xylene are conducted in a newly designed three-sides optically accessible scavange constant volume chamber (CVC).

Fig. 1 shows the setup of the experimental system as well as other related experimental apparatus. The CVC is a cuboid chamber with the internal dimension of $50 \times 50 \times 270 \text{ mm}^3$. Quartz windows are mounted on three surrounding surfaces of CVC. One narrow window is equipped for the laser sheet/

Table 1 Thermodynamic properties of *p*-xylene, *n*-octane and gasoline at 0.1 MPa

Chemical formula	C_8H_{10} [32]	C_8H_{18} [32]	Gasoline (C_4-C_{12}) [35]
Density at 293 K (kg/m^3)	857	699	720–740
Boiling point (K)	411.5	398.5	308–473
Kinematic viscosity $\times 10^{-6}$ (m^2/s)	0.706	0.737	0.53
Enthalpy of vaporization at 298 K (kJ/kg)	399.4 [33]	366.8 [34]	420

Fig. 1 Schematic of the optical and experimental setup



beam access, and another two parallel windows are allowing fluorescence imaging or absorption measurements. On the fourth surrounding face, thermocouple locates inside the chamber and detects the temperature of the CVC central position. On the top of CVC, the pressure sensor and gaseous flow outlet are arranged. The gaseous flow inlet lies on the bottom of the CVC and along with its downstream the flow passes through an 8-hole straightener panel to generate a homogenous flow field inside the chamber. The operation limitation of pressure and temperature for this CVC reaches 10 MPa and 800 K, respectively.

The gaseous supply and heating system comprises from the N₂ tank to the premixed-tank, as labeled from 18 to 12 in Fig. 1. In the experiments, the carrier gas nitrogen comes from N₂ tanks (99.99% stated purities) and its flow rate is adjusted by a Bronkhorst EL-FLOW mass flow controller (16). Afterward, the nitrogen is heated by two electrical resistance heaters (13) and introduced into the bottom of the premixed-tank (12). The temperature of the N₂ is higher than the boiling point of *p*-xylene but lower than its pyrolysis temperature. Meanwhile, the liquid *p*-xylene (purity >99.99%, Aladdin) is injected into the premixed-tank (from the top of premixed-tank) under superheated condition by a 6-hole nozzle injector to complete flash-boiling process and fully mixes with heated nitrogen in the premixed-tank. Within this injection process, the liquid *p*-xylene is constantly heated up to 433 K that enabled by an oil bath system, which allows for the flash-boiling spray achievement. The injector applied in this study is operated at proper parameters (injection pressure: 5 MPa, injection frequency: 10 Hz and injection duration: 1000 μs). Through such heater strategy and injection protocol, the liquid *p*-xylene depositing on the wall of premixed-tank and vapor *p*-xylene degradation are avoided, which guarantees accurate gaseous *p*-xylene concentration supply. Doing so, the *p*-xylene and nitrogen could be mixed uniformly and heated to the required temperature before they enter into the CVC. More specifically, the uncertainty of *p*-xylene injection is 0.3% and the controlled temperature and pressure uncertainties are 0.5 and 1%, respectively. Overall, the possible *p*-xylene concentration variation with time is 1.15%. Moreover, the forwarding data processing of temperature validation is a statistic result in the ROI (ref. Sect. 3.3), thus, this statistical result could well represent the targeted experimental condition (number density, pressure and temperature) and the *p*-xylene concentration variation (1.15%) is negligible, even with some random variation existing. Therefore, under our each experimental condition, it is assumed that the gaseous supply system creates a uniform field in terms of temperature and concentration at a steady-state condition in the CVC.

The light source of the optical diagnostic system is composed of a Nd:YAG laser (Spectra Physics Quanta-Ray, 266 nm, 90 mJ/pulse at 10 Hz) for the fluorescence measurements

and a Deuterium–Halogen lamp (model DH-2000, Ocean Optics, large emission spectrum from 215 to 2500 nm) coupled to an optical fiber for the absorption spectrum measurements. In the fluorescence spectrum and fluorescence field measurements, the output of the Nd:YAG laser is a beam with 8 mm diameter (70 mJ/pulse) and then it is formed into a light sheet of about 20 mm height and a thickness of 1 mm by a convex lens ($f = 1000$ mm) and a cylindrical lens ($f = -60$ mm). After the light sheet passes through the test area, fluorescence emission image was collected perpendicular to the laser sheet by a Nikon $f = 105$ mm, $f_{\#} = 4.5$ UV camera lens and imaged on an ICCD camera (PI, PIMAX 1024 × 1024 pixels², 16 bytes of dynamic range). The 289 nm bandpass filter (Edmund, 25 mm diameter, FWHM = 10 nm, OD >4), 320 nm bandpass filter (Edmund, 25 mm diameter, FWHM = 10 nm, OD >4) and 340 nm bandpass filter (Edmund, 50 mm diameter, FWHM = 10 nm, OD >4) are installed before the UV lens for the measurement of spectral fluorescence signal field, respectively. Simultaneously, fluorescence spectrum from part of the illuminated *p*-xylene vapor is collected at another right angle via a spectrometer (Ocean Optics, QEPro, entrance slit fixed at 50 μm with spectral resolution of 1 nm). Within the same gaseous supply and spectrometer arrangement, the *p*-xylene absorption spectrum could be performed through replacing the ICCD by the light source of Deuterium–Halogen lamp.

3 Results and discussion

3.1 *p*-Xylene absorptions

The absorption cross section of *p*-xylene is evaluated via the Beer's–Lambert law by Eq. (1):

$$\sigma(\lambda) = \frac{\ln[I_0(\lambda)/I(\lambda)]}{l \times C}. \quad (1)$$

Here, I_0 is the incident laser intensity; I is the detected transmitted intensity; l is the light source probed path length (cm), and C is the *p*-xylene number density (molecule/cm³). All these parameters are specified by the defined experimental condition. In our study, using temperature range from 423 to 623 K with pressure of 0.2 MPa, the measurements represent 3.1×10^{17} to 1.8×10^{17} molecule/cm³ of *p*-xylene in number density.

Figure 2 shows the measured *p*-xylene vapor spectral absorption cross-section variation with the temperature range from 423 to 623 K. As expected, at the low temperature of 423 K, two absorption peaks approximately at 265 and 275 nm could be identified. By increasing temperature, the losing of the fines structures of absorption spectrum is found. Similar results were reported in the studies of toluene and anisole, which could be explained by thermally assisted

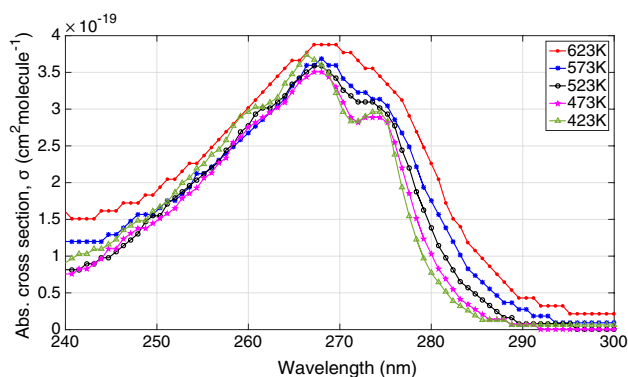


Fig. 2 Absorption cross section of *p*-xylene for different temperatures in nitrogen at 0.2 MPa

of excited state population [10, 27]. A typical absorption cross-section magnitude comparison at 266 nm with frequently studied tracers is listed in the last column of Table 2. As anticipated, the absorption cross section of *p*-xylene is between that of toluene and TMB. The larger the absorption cross section, the less number density is required for the higher SNR.

Furthermore, a closer quantitative study of absorption cross-section variation with temperature deserves further investigation and comparison. By the observation of Fig. 2, below the wavelength of 270 nm, the absorption cross section has an ambiguous dependence within performed temperature range, while above 270 nm, it increases with temperature rising. As a result, by the 266 nm wavelength excitation, the *p*-xylene σ shows an overall increasing trend by a mean value of $(3.4 \pm 0.2) \times 10^{-19} \text{ cm}^2/\text{molecule}$ within our studied temperature range in N_2 . Noted that in the wing part of absorption spectrum (above 270 nm for *p*-xylene and toluene, cf. Fig. 3 in [10], above 280 nm for anisole, cf. Fig. 4 in [27]), all these tracers show σ clearly monotonic increasing with temperature rising, which maybe caused by temperature broadening [36, 37].

In addition, the energy gap between the origin of the S_1 state and excitation photon energy seems correlated to the absorption cross-section variation with temperature. Table 2 summaries the S_1 state zero band, the excess energy by the

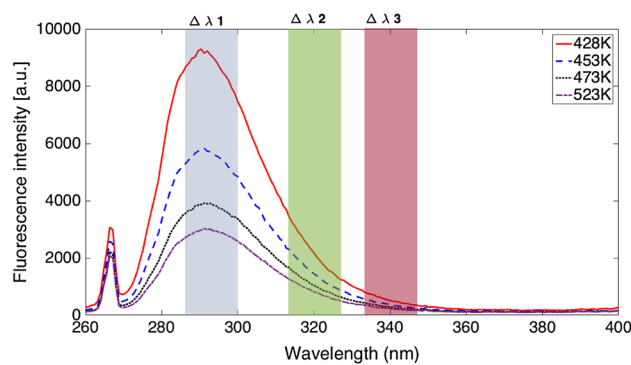


Fig. 3 Evolution of *p*-xylene fluorescence spectrum in nitrogen at 0.2 MPa excited by 266 nm within different temperatures

266 nm laser excitation (i.e., a photon with energy 37594 cm^{-1}) and the absorption cross-section correlation with temperature of some tracers that existing in the references.

As we can see from the third column in the Table 2, it clearly indicates that with rising of vibrational excess energy, the σ firstly shows a positive response to temperature, then negative correlation and final the uncorrelated with temperature. This potential correlation is interpreted as following: when excess energy becomes larger, the vibrational energy distribution of the ground state molecules becomes more insignificant for the population to the first excited state, i.e. thermally assisted population is not relevant [37]. For instance, for toluene excited at 248 nm with an excess energy of 2846 cm^{-1} , a nearly constant absorption cross-section from room temperature up to 1000 K is also reported [10]. It is worth mentioning that this offers a reasonable explanation for the absorption cross-section dependence on temperature, the further investigation is deserved to approach addressing the issue, which is out of this paper's scope.

3.2 *p*-Xylene fluorescence

Fig. 3 represents the experimentally measured *p*-xylene fluorescence spectrum in nitrogen at 0.2 MPa excited at 266 nm within temperature range from 428 to 523 K. Indeed, since the flowrate of nitrogen increases when temperature rises at fixed pressure, the fluorescence spectra of *p*-xylene have

Table 2 Five tracers' temperature dependence of absorption cross section by 266 nm laser excitation

Tracer	S_1 (0, 0) band (cm^{-1})	Excess energy (cm^{-1})	σ Response to temp.	Absorp. cross-section (266 nm)/(10^{-20} cm^2)
Toluene	37476 [38]	117	Monotonic increasing [10]	19 (298 K) [10]
<i>p</i> -Xylene	36732 [38]	861	Overall increasing	34 (423 K)
1,2,4-TMB	36435 [38]	1158	Monotonic decreasing [19]	135 (298 K) [37]
Anisole	36384 [39]	1209	Monotonic decreasing [27]	701.3 (573 K) [27]
Naphthalene	32020 [22]	5574	Constant [22]	1400 (298 K) [11]

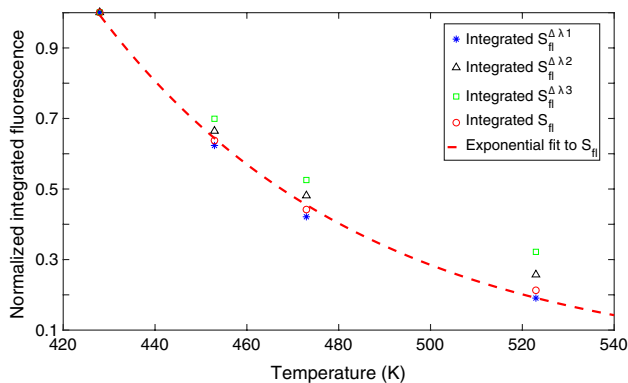


Fig. 4 Variations of integrated spectral fluorescence intensity with temperature in nitrogen at 0.2 MPa excited at 266 nm. All the profiles are normalized to respective fluorescence intensity at temperature of 428 K. (Blue star: integrated fluorescence within spectral band centred at $\lambda_1=289$ nm; black triangle: integrated fluorescence within spectral band centred at $\lambda_2=320$ nm; green square: integrated fluorescence within spectral band centred at $\lambda_3=340$ nm; red circle: integrated entire fluorescence spectrum)

been corrected for reduction in number density. However, the fluorescence measurements were carried out under the fluorescence linear regime. In the fluorescence spectrum profiles, the first peak is related to the laser intensity at 266 nm, while the second fluorescence peak is around at 290 nm. Fluorescence intensity peak decreases by a factor of 3 when the temperature increases 100 K, due to a high non-radiative decay rate of excited state at higher temperatures. This feature underlines the interest of *p*-xylene as a tracer for the measurement of temperature by PLIF. It is worth noting that the fluorescence self-quenching incurred by the number density is neglected in this studies. The potential influence of the self-quenching on fluorescence spectra and the final temperature determination deserves further investigation, which is enlightened by the recently toluene self-quenching studies [40].

Fig. 4 demonstrates the variations of the integrated spectral fluorescence intensity with temperature, which have already been indicated by the shadow areas in Fig. 3. The three spectral bands are $\Delta\lambda_1=284\text{--}294$ nm, $\Delta\lambda_2=315\text{--}325$ nm and $\Delta\lambda_3$

= 335–345 nm, respectively. All these temperature evolutions follow the exponential decay.

The methodology and application of single-excitation, single-color detection technique for temperature measurements have been extensively discussed in previous studies [27, 30, 41]. And its application is confined to operating conditions of constant pressure and homogeneous tracer distribution in the detected volume. As a complementary results, Fig. 4 (red circle) shows the variation of integrated entire *p*-xylene fluorescence spectrum (270–400 nm) with the temperature as well. Therefore, the following fitted exponential expression (red dash line) can be deduced:

$$\frac{\phi(T)}{\phi(428\text{ K})} \Big|_{266\text{ nm}} = 1659 \times \exp(-0.01734T). \tag{2}$$

In other words, the temperature is inferred from the FQY:

$$T = -57.67\ln(\phi) + 427.56. \tag{3}$$

Similar experimental temperature correlations from other tracers in the literature are listed in Table 3.

3.3 Temperature field measurements by *p*-xylene PLIF technique

Another widely applied temperature measurement technique based on fluorescence signal is the single-excitation two-color detection method, since it enables to measure fluorescence signal in inhomogeneously seeded field and using of simple equipment [27, 30]. The brief reminding could be well represented as following equation:

$$\frac{S_f^{\Delta\lambda_1}(x, y, T, P)}{S_f^{\Delta\lambda_2}(x, y, T, P)} = \frac{\eta_{\text{opt}}^{\Delta\lambda_1} E(x, y) n_{\text{tracer}}(x, y) \sigma(T) \phi^{\Delta\lambda_1}(T, P)}{\eta_{\text{opt}}^{\Delta\lambda_2} E(x, y) n_{\text{tracer}}(x, y) \sigma(T) \phi^{\Delta\lambda_2}(T, P)}. \tag{4}$$

The left of the equation shows the ratio between the fluorescence signal detected on the spectral bands $\Delta\lambda_1$ and $\Delta\lambda_2$, which are obtained directly from planar fluorescence measurements; x and y are two-dimensional parameters of the laser probed volume; On the right side, the $\eta_{\text{opt}}^{\Delta\lambda}$ is the overall efficiency of the collection optics within spectral bands; $E(x, y)$ is the laser energy; $n_{\text{tracer}}(x, y)$ is the local tracer

Table 3 Summaries of temperature correlations of different tracers that employed for temperature measurements through single-excitation, single-color detection technique

Author	Experimental temp. correlation	Conditions
Current work	$T = -57.67\ln(\phi) + 427.56$	<i>p</i> -Xylene excited at 266 nm in N ₂ $T = 428\text{--}523$ K, $P = 0.2$ Mpa
Tran et al. [27]	$T = -108.69\ln(\phi) + 469.56$	Anisole excited at 266 nm in N ₂ $T = 473\text{--}823$ K, $P = 0.2$ Mpa
Koban et al. [42]	$T = -92.5\ln(\phi) + 296.5$	Toluene excited at 266 nm in N ₂ $T = 300\text{--}950$ K, $P = 0.1$ Mpa
Luong et al. [41]	$T = -57.895\ln(\phi) + 289.08$	Toluene excited at 248 nm in N ₂ $T = 300\text{--}923$ K, $P = 0.1$ Mpa
Kühni et al. [30]	$T = -89.294\ln(\phi) + 452.91$	Fluoranthene excited at 266 nm in N ₂ $T = 473\text{--}873$ K, $P = 0.1$ Mpa

density; $\sigma(T)$ is the absorption cross section of tracer and $\phi^{\Delta\lambda}(T, P)$ is the spectral integrated FQY at specific temperature and pressure, which also could be obtained by fluorescence spectrum measurements.

Therefore, at specific pressure within each probed point, tracer density, laser energy and absorption cross section are identical for two spectral bands, Eq. (4) is simplified as:

$$\frac{S_f^{\Delta\lambda_1}(x, y, T, P_{fix})}{S_f^{\Delta\lambda_2}(x, y, T, P_{fix})} \propto \frac{\eta_{opt}^{\Delta\lambda_1}(x, y)\phi^{\Delta\lambda_1}(T(x, y), P_{fix})}{\eta_{opt}^{\Delta\lambda_2}(x, y)\phi^{\Delta\lambda_2}(T(x, y), P_{fix})} = f(T(x, y)). \tag{5}$$

As a result, the temperature correlation to the ratio of integrated spectral fluorescence could be established as temperature calibration database by fluorescence spectrum measurements. Consequently, the probed field temperature could be inferred by knowing the two local spectral fluorescence signal intensity ratio. In the above theoretical methodology explanations, $\Delta\lambda_1$ and $\Delta\lambda_2$ represent two of those wavelength band $\Delta\lambda$ ($\Delta\lambda_1, \Delta\lambda_2, \Delta\lambda_3$).

The accuracy of calibration curve is one of the major factors that affect the final temperature solution. Experimentally, the spectral transmission variation of the bandpass filters and the spectral response of the ICCD are considered as the two major factors inducing the η_{opt} divergence that modifies temperature-ratio calibration curves. Thus, other optical efficiencies influence is taken into account in the calibration, e.g., the collecting solid angle. Fig. 5 shows the transmissions of three selected bandpass filters and quantum efficiency of ICCD that incorporated in our optical detecting system. Because of the low quantum efficiency of ICCD at 289 nm, the wing fluorescence at 340 nm was studied in present article. Therefore, three spectral bands that respective centred at 289, 320 and 340 nm are proposed to establish the calibration data. As a result, based on the spectral fluorescence integrated results in Fig. 4 and the optical parameters in Fig. 5, Fig. 6 presents the calculated three calibration

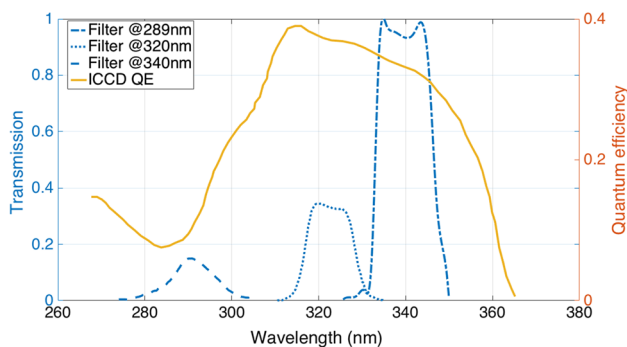


Fig. 5 The variation of three UV filter transmission and ICCD quantum efficiency within different wavelengths

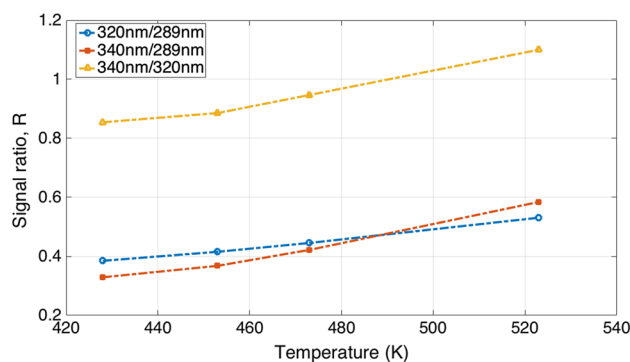


Fig. 6 Three calibration curves R obtained from different spectral bands combination

curves, namely, variation of the integrated spectral fluorescence intensity ratio (R) with the temperature.

The spectral band combination optimization is another essential factor, which affects the final temperature measurement accuracy. It could be a compromise choice between the temperature detection sensitivity and the SNR. By the normalized sensitivity analysis ($1/R dR/dT \sim T$) referred from Fig. 6, it indicates that the spectral band ratio of 340/289 nm has the largest sensitivity in studied temperature range, in other words, that spectral band combination enables the best temperature accuracy solution. However, the SNRs of the different fluorescence signal at 289, 320 and 340 nm are required to be further considered for the spectral band combination optimization.

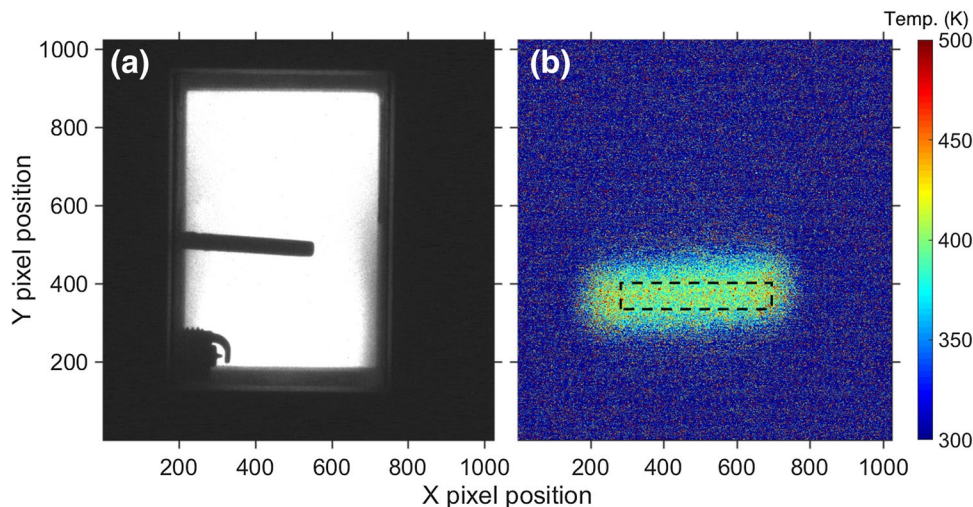
To this end, the temperature field measured through these three band combinations (320/289 nm, 340/289 nm and 340/320 nm) are implemented. The detailed experimental setup and procedures have been described in Sect. 2.2. Table 4 presents the summaries of the experimental parameters for temperature field measurements. In this set of experiments, the laser fluence keeps constantly at 70 mJ/pulse to format the laser sheet. The gaseous *p*-xylene and N_2 mixture temperature rise from 423 to 573 K through controlling of electrical resistances heater and flowrate, which is monitored by the thermocouple located in CVC. Concomitantly, the spectral fluorescence field images that centred at 289, 320 and 340 nm are recorded, respectively.

The Fig. 7a exhibits the focused optical window that captured by ICCD camera, which indicates the thermocouple position and excellent ICCD sensor resolution due to clear distinguishing of the gap between the spark plug electrodes. As an example, the typically inferred temperature field through fluorescence signal 340/289 nm ratio at condition of 423 K and 0.2 MPa that scaled by the original ICCD sensor pixels, as shown in Fig. 7b. It should be noted that under every temperature condition the spectral fluorescence image ($LIF^{\Delta\lambda}(x, y)$) was averaged from 30 frames. An equivalent set of measurements was also acquired forwards with the same laser energy in the cell

Table 4 The experimental conditions for temperature field measurement by *p*-xylene PLIF technique

Constant parameters			Variation parameters		
Laser fluence (mJ/pulse)	Pressure (MPa)	Pixel size of ROI	Temperature (K)	Number density (molecule/cm ³)	Flow rate (L/min)
70	0.2	<i>X</i> range: 310–670 <i>Y</i> range: 352–407	423	5.29 × 10 ¹⁷	70
			448	5.23 × 10 ¹⁷	70
			473	4.74 × 10 ¹⁷	80
			523	3.69 × 10 ¹⁷	108
			573	3.71 × 10 ¹⁷	121

Fig. 7 **a** The focused laser sheet accessible optical window image captured by the ICCD camera. **b** Temperature map inferred from the signal ratio of 340/289 nm at condition of 423 K and 0.2 MPa. Both the images are scaled by the original ICCD sensor pixels. The black dash rectangle is the delineated ROI



evacuated from any *p*-xylene vapor to allow subtraction of background light from fluorescence (Laser^{Δλ}_{background}(*x, y*)).

The post-processing for temperature field that referring from ratio field follows the Eq. (6):

$$T(x, y) \propto \text{Ratio}(x, y) = \frac{\frac{1}{N} \sum_i^N \text{LIF}^{\Delta\lambda 1}(x, y) - \frac{1}{N} \sum_i^N \text{Laser}_{\text{background}}^{\Delta\lambda 1}(x, y)}{\frac{1}{N} \sum_i^N \text{LIF}^{\Delta\lambda 2}(x, y) - \frac{1}{N} \sum_i^N \text{Laser}_{\text{background}}^{\Delta\lambda 2}(x, y)}$$

number : *N* = 30.

(6)

To assess the suitability and accuracy of the measured temperature fields through the three spectral band combinations, the identical region of interest (ROI) is delineated for every temperature results to carry out the quantitative analysis. The ROI encompasses the illuminated area on the laser sheet propagation direction (−*X* direction) and the boundaries of pixel in *x* scale and *y* scale are 310–670 and 352–407, as shown by black dash rectangle on Fig. 7b.

$$T_{\text{average}} = \frac{1}{19800} \sum_{i=310}^{670} \sum_{j=352}^{407} T(x_i, y_j). \tag{7}$$

Therefore, the calculation of total 19800 (360 × 55) pixels’ average temperature by Eq. (7) is chosen to represent the measured temperature through different spectral band combinations. However, for avoiding unrealistic temperature incurred from experimental image ratio processing, the selection of inferred temperature for that calculation is identified by not only the pixels inside this ROI, but also a reasonable range of ratio itself. Inspecting the curves in Fig. 6 leads to the following ratio range criteria:

$$0.3 \leq \frac{S_f^{320 \text{ nm}}(x, y)}{S_f^{289 \text{ nm}}(x, y)} \leq 1 \tag{8}$$

$$0.3 \leq \frac{S_f^{340 \text{ nm}}(x, y)}{S_f^{289 \text{ nm}}(x, y)} \leq 1 \tag{9}$$

$$0.5 \leq \frac{S_f^{340 \text{ nm}}(x, y)}{S_f^{320 \text{ nm}}(x, y)} \leq 1.5 \tag{10}$$

As a result, at every experimental temperature condition from 423 to 573 K, three average temperatures are obtained

through that of respective spectral band combination. The scatter points in Fig. 8 display its variation with the temperature. Since the ROI is merely beneath the thermocouple tip, the temperature indicated by the thermocouple well represents the real temperature that measured by *p*-xylene PLIF. Thus, the discrepancies between the calculated average temperature by three spectral band combinations and that of measured by the thermocouple (black line in Fig. 8) indicate the temperature measurement accuracy through *p*-xylene PLIF technique.

Compared to other two spectral band combinations, the combination of 320/289 nm provides the best temperature measurement precision within the studied temperature range. The error bar implies the measurement uncertainties, which are composed of the thermocouple measurement uncertainties (± 2.5 K) and the measured temperature discrepancy between thermocouple and 320/289 nm ratio of PLIF. As a result, an average relative error of 2.6% is obtained within the studied temperature range from 423 to 573 K. Indeed, the 340/289 nm or 340/320 nm combination also offers acceptable temperature performance in the low temperature range. Since the fluorescence signal intensity at 340 nm substantially drops at high temperature, to be more specific, the SNR reduces approximately from 15 to 5, while the temperature increases to 150 K. Therefore, the large temperature discrepancy at 573 K is mainly attributed to the low SNR and the uncertainties of calibration procedures.

However, the mentioned uncertainties reveal a better temperature resolution with the previous studies in the reference, e.g., a 5.5% temperature uncertainty of 600 K via toluene-based, one-line, two-color PLIF technique was reported by Luong et al. [43]. Through the same technique approach, a similar relative error of 5% at 500 K was reported by Cundy et al. [16]. On the other hand, through the 3-pentanone-based two-line PLIF technique, Einecke et al. [13] reported

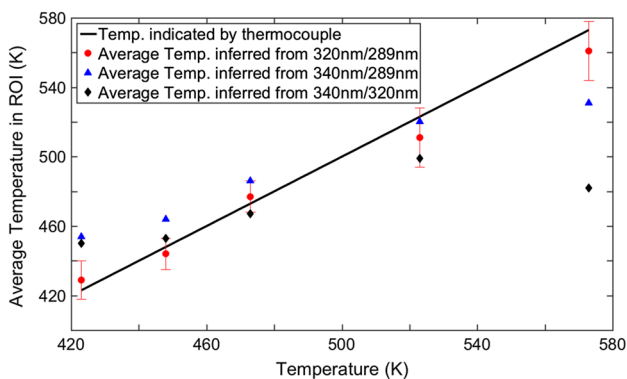


Fig. 8 Comparisons of the thermocouple indicated temperature and the calculated average temperature through three spectral band combinations by *p*-xylene PLIF. The error bar implies the temperature measurement uncertainties through 320/289 nm spectral band combination

a relative error of approximately 4% in temperature at 600 K. More recently, Rothamer et al. [44] further optimized the two-line approach and thus, the reported error was reduced to 2.1%. It is reasonable that the two-line excitation offers the better temperature solution than the one-line excitation, because of the complexity of two-line excitation.

In addition, as expected, the laser intensity will be attenuated on the laser propagation direction since its energy is absorbed by the *p*-xylene molecules on the laser pathway. As a result, it is normal that the attenuated spectral fluorescence intensity image on the laser pathway are observed in our experiments. Interestingly, the measured temperature along the $-X$ direction has not been largely impaired by this laser attenuation, which is evidenced by the temperature field shown in Fig. 7b. This result further supports the suitability and robustness of the temperature field measurement by the *p*-xylene PLIF technique.

4 Conclusions

In this study, the absorption cross-section characteristics and fluorescence spectra of *p*-xylene within temperature range from 423 to 623 K at pressure of 0.2 MPa are well studied and documented. The absorption cross section of *p*-xylene at 266 nm shows a mean value of $(3.4 \pm 0.2) \times 10^{-19}$ cm²/molecule within previous mentioned temperature range, whereas the energy gap between the origin of the S_1 state and excitation photon energy correlated to the absorption cross-section response to temperature is revealed. The suitability and accuracy of *p*-xylene used as a temperature indicator in the vapor field through the single excitation (at 266 nm) two-color detection LIF technique is analyzed and validated for the first time. It turns out fluorescence spectral bands of 320/289 nm combination offers the best temperature solution of relative error of 2.6% within our studied temperature range, while the measured temperature accuracy degradation of 340/289 nm or 340/320 nm combination at high temperature condition is mostly due to the low SNR and uncertainty of calibration procedures. It is interesting to find that the measured temperature field has not been largely impaired by the laser attenuation on its propagation direction, which further supports the robustness of the temperature field measurement by the *p*-xylene PLIF technique.

Acknowledgements The present study has been supported by the China Postdoctoral Science Foundation (No. 2016M591672), Innovation Program of Shanghai Municipal Education Commission (No. 14ZZ022) and Science and Technology Project of Guangdong Province (No. 2016A040403095). Key Laboratory of Hypersonic Ramjet Technology of China (No. STS/MY-KFKT-2014001). The authors feel grateful to Wenyuan Qi, Qingzhe Zhou and engineer of Yuanming Ma for their contributions to the establishment of the experimental setup.

References

1. H. Oh, C. Bae, *Fuel* **107**, 225–235 (2013)
2. J. Serras-Pereira, P.G. Aleiferis, D. Richardson, *Combust. Sci. Technol.* **185**, 484–513 (2013)
3. L.A. Melton, *Appl. Opt.* **22**, 2224–2226 (1983)
4. A.M. Murray, L.A. Melton, *Appl. Opt.* **24**, 2783–2787 (1985)
5. P. Wieske, S. Wissel, G. Grunefeld, S. Pischinger, *Appl. Phys. B* **83**, 323–329 (2006)
6. T.D. Fansler, M.C. Drake, *Meas. Sci. Technol.* **20**, 125401 (2009)
7. A.P. Froba, F. Rabenstein, K.U. Munch, A. Leipertz, *Combust. Flame* **112**, 199–209 (1998)
8. H. Chen, M. Xu, G. Zhang, M. Zhang, Y. Zhang, A.S.M.E. Conf. Proc. **49446**, 391–403 (2010)
9. M.C. Thurber, R.K. Hanson, *Appl. Phys. B* **69**, 299 (1999)
10. W. Koban, J. Koch, R. Hanson, C. Schulz, *Phys. Chem. Chem. Phys.* **6**, 2940 (2004)
11. J.D. Koch, J. Gronki, R.K. Hanson, *J. Quant. Spectrosc. Radiat. Transf.* **109**, 2037 (2008)
12. J.D. Koch, R.K. Hanson, *Appl. Phys. B* **76**, 319 (2003)
13. S. Einecke, C. Schulz, V. Sick, *Appl. Phys. B* **71**, 717–723 (2000)
14. L. Zigan, J. Trost, A. Leipertz, *MTZ Worldwide* **75**, 50–55 (2014)
15. B.H. Cheung, R.K. Hanson, *Appl. Phys. B* **98**, 518 (2010)
16. M. Cundy, P. Trunk, A. Dreizler, V. Sick, *Exp. Fluids* **51**, 1169 (2011)
17. J. Yoo, D. Mitchell, D.F. Davidson, R.K. Hanson, *Exp. Fluids* **49**, 751 (2010)
18. S. Faust, T. Dreier, C. Schulz, *Chem. Phys.* **383**, 6 (2011)
19. M. Orain, P. Baranger, B. Rossow, F. Grisch, *Appl. Phys. B* **100**, 945–952 (2010)
20. S. Faust, G. Tea, T. Dreier, C. Schulz, *Appl. Phys. B* **110**, 81 (2013)
21. S. Kaiser, M. Long, *Proc. Combust. Inst.* **30**, 1555 (2005)
22. M. Orain, P. Baranger, B. Rossow, F. Grisch, *Appl. Phys. B* **102**, 163–172 (2011)
23. R. Zhang, V. Sick, SAE Technical Paper 2007-01-1826, (2007)
24. B. Williams, P. Ewart, X. Wang, R. Stone, H. Ma, H. Walmsley, R. Cracknell, R. Stevens, D. Richardson, H. Fu, S. Wallace, *Combust. Flame* **157**, 1866–1879 (2010)
25. G. Tea, G. Bruneaux, J.T. Kashdan, C. Schulz, *Proc. Combust. Inst.* **33**, 783–790 (2011)
26. S. Lind, U. Retzer, S. Will, L. Zigan, *Proc. Combust. Inst.* **36**, 4497–4504 (2017)
27. K.H. Tran, C. Miron, M. Kühni, P. Guibert, *Appl. Phys. B* **115**, 461–470 (2014)
28. S. Faust, T. Dreier, C. Schulz, *Appl. Phys. B* **112**, 203 (2013)
29. Q. Wang, K.H. Tran, C. Morin, J. Bonnetty, G. Legros, P. Guibert, *Appl. Phys. B* **123**, 199 (2017)
30. M. Kühni, C. Morin, P. Guibert, *Appl. Phys. B* **102**, 659–671 (2011)
31. K. K. David, J. S. Klaus, *Spring GWMR*, 135–145 (1990)
32. Y. Zhang, K. Nishida, *Combust. Sci. Technol.* **179**, 863–881 (2007)
33. A.G. Osborn, D.R. Douslin, *J. Chem. Eng. Data* **19**, 114–117 (1974)
34. M. Michou-Saucet, J. Jose, *Thermochim. Acta* **75**, 85–106 (1984)
35. L. Zigan, I. Schmitz, *Fuel* **90**, 348–363 (2011)
36. I.S. Zaslanko, *Rus. Chem. Rev.* **6**, 483–507 (1997)
37. B. Rossow, Ph.D. Thesis, Universite of Paris-sud 11, 191 (2011)
38. A. Bolovins, J. Philis, E. Pantos, G. Andritsopoulos, *J. Mol. Spectrosc.* **94**, 55–68 (1982)
39. R. Matsumoto, K. Sakeda, Y. Matsushita, T. Suzuki, T. Ichimura, *J. Mol. Struct.* **735–736**, 153–167 (2005)
40. D. Fuhrmann, T. Benzler, S. Fernando, T. Endres, T. Dreier, S.A. Kaiser, *Proc. Combust. Inst.* **36**, 4505–4514 (2017)
41. M. Luong, W. Koban, C. Schulz, *J. Phys.* **45**, 133–139 (2006)
42. W. Koban, J. Koch, R. Hanson, C. Schulz, *Appl. Phys. B* **80**, 777–784 (2005)
43. M. Luong, R. Zhang, C. Schulz, V. Scik, *Appl. Phys. B* **91**, 669–675 (2008)
44. D.A. Rothamer, J.A. Snyder, R.K. Hanson, R.R. Steeper, *Appl. Phys. B* **99**, 371–384 (2010)